Flare Plasma Cooling from 30 MK down to 1 MK modeled from Yohkoh, GOES, and TRACE observations during the Bastille-Day Event (2000 July 14) *

Markus J. Aschwanden and David Alexander
Lockheed Martin Advanced Technology Center, Solar and Astrophysics Laboratory, Dept. L9-41, Bld.252., 3251 Hanover St., Palo Alto, CA 94304, USA

Abstract. We present an analysis of the evolution of the thermal flare plasma during the 2000-Jul-14, 10 UT, Bastille-Day flare event, using spacecraft data from Yohkoh/HXT, Yohkoh/SXT, GOES, and TRACE. The spatial structure of this double-ribbon flare consists of a curved arcade with some 100 post-flare loops which lighten up in a sequential manner from highly-sheared low-lying to less-sheared higher-lying bipolar loops. We reconstruct an instrument-independent, average differential emission measure distribution $dEM(T)/dT$ that ranges from $T = 1$ MK to 40 MK and peaks at $T_0 = 10.9$ MK. We find that the time profiles of the different instrument fluxes peak subsequently over 7 minutes with decreasing temperatures from $T \approx 30$ MK to 1 MK, indicating the systematic cooling of the flare plasma. From these temperature-dependent relative peak times $t_{peak}(T)$ we reconstruct the average plasma cooling function $T(t)$ for loops observed near the flare peak time, and find that their temperature decrease is initially controlled by conductive cooling during the first 188 s, $T(t) = T_2[1 + (t/\tau_{cond})]^{-2/7}$, and then by radiative cooling during the next 592 s, $T(t) = T_1[1 - (t/\tau_{rad})]^{3/5}$. From the radiative cooling phase we infer an average electron density of $n_e = 4.2 \times 10^{11}$ cm^{-3}, which implies a filling factor near 100% for the brightest observed 23 loops with diameters of ≈ 1.8 Mm that appear simultaneously over the flare peak time and are fully resolved with TRACE. We reproduce the time delays and fluxes of the observed time profiles near the flare peak self-consistently with a forward-fitting method of a fully analytical model. The total integrated thermal energy of this flare amounts to $T_{thermal} = 2.6 \times 10^{31}$ erg.

Keywords: solar flares - thermal emission - hard X-rays - soft X-rays - EUV - plasma cooling

1. Introduction

The Bastille-Day flare of 2000-Jul-14, one of the largest flares of this solar cycle, is one of the best-observed flare events on record: with comprehensive coverage of the temperature range in soft X-rays and extreme ultraviolet wavelenghts (EUV), with good time resolution from 0.5 s in hard X-rays, 3 s to minutes in soft X-rays, and minutes in EUV, and with excellent spatial resolution, from 1" in EUV to 2.5" in soft X-rays. We make use of spacecraft data in hard X-rays from

* SOLAR PHYSICS special issue on Bastille Flare.

the Yohkoh Hard X-ray Telescope (HXT), soft X-ray data from the Yohkoh Soft X-ray Telescope (SXT) and the Geostationary Satellite (GOES), and EUV data from the Transition Region and Coronal Explorer (TRACE). The quality and excellent temperature coverage of the data lend themselves naturally to a comprehensive study of the evolution of the thermal behaviour of the flare.

The energy release mechanism of this flare is generally assumed to follow the Kopp and Pneuman (1976) magnetic reconnection model, due to the observed classical double-ribbon features. A magnetic instability is supposed to take place above the magnetic neutral line, accompanied by a coronal mass ejection, which is also evidenced as dimming of the EUV brightness by TRACE at the beginning of the flare above the western part of the flare arcade. The magnetic reconnection results in the acceleration of nonthermal particles which precipitate down to the two flare ribbons north and south of the neutral line. The precipitation sites of nonthermal particles along the two flare ribbons are for the first time mapped as ribbon-like features in hard X-rays during this flare (Masuda et al., 2001). As a result, chromospheric evaporation ensues and gradually fills the newly-reconnected coronal field lines, called flare loops, with hot, dense plasma shortly after the peak of the flare. The thermal evolution suggests a progressive cooling of the plasma which is first evident in the hottest plasma with temperatures of $T \approx 30 - 40$ MK that flows up with a low emission measure, detectable in the Yohkoh/HXT Lo channel (14-23 keV). Hot plasma with temperatures of 20-30 MK but higher emission measure peaks a few minutes later in the GOES data. This is followed a few minutes later when we register the largest amount of upflowing plasma with temperatures of 10-20 MK with Yohkoh/SXT. About 13 minutes after the first detectable upflow the plasma has cooled down to EUV temperatures of 1-2 MK, which we detect with TRACE. Of course, the whole process repeats in every identified flare loop, approximately 100 in number, with a different timing, so that we can only determine the plasma cooling function of a single flare loop by deconvolving the multi-wavelength observations. We determine the average plasma cooling function $T(t)$ for this flare and find that conductive cooling dominates in the initial phase, while radiative cooling dominates the major part of its cooling phase at later times. We find that a cooling cycle of an average loop from $T \approx 30$ MK down to 1 MK lasts about 13 minutes, but is assumed to repeat in each of the 100 loops observed during the first hour of the flare. The observations also demonstrate that the first newly-reconnected field lines are highly sheared and low-lying above the neutral line, while the later reconnected field lines are less sheared and are located higher above the neutral line, as expected

from the standard (Kopp and Pneuman, 1976) model due to the upward motion of the reconnetion region. Along with this evolution, we witness also an increasing separation of the flare ribbons with time, another prediction of the (Kopp and Pneuman, 1976) model. All in all, this flare confirms the standard reconnection model that emerged from the work of (Kopp and Pneuman (1976), Carmichael (1964), Sturrock (1966), Masuda (1994), Tsuneta et al. (1996) in remarkable detail.

2. Data Analysis

Our data analysis includes imaging data from Yohkoh/HXT, Yohkoh/SXT, and TRACE, as well as light curves from GOES.

2.1. Yohkoh/HXT Observations

The Yohkoh HXT (Kosugi et al., 1991) imaged the Bastille-Day flare from 2000-Jul-14, 10:11:12-10:56:22 UT, with a data gap during the rise time of the flare, between 10:13:12 and 10:19:36 UT, due to ground-station contact for telemetry downlinking. The time resolution during flare mode was 0.5 s. The time profiles of the total hard X-ray flux $F_{HXR}(t)$ in the four energy channels 14-23 keV (Lo), 23-33 keV (M1), 33-53 keV (M2), and 53-93 keV (Hi) are shown in Fig.1 (top). We assume that the low HXT channel is completely dominated by thermal emission, as the absence of pronounced fast time structures (seen in the high-energy HXT channels) and the similarity of the HXT/Lo time profile with the entirely thermal emission observed in SXT/Be suggests (Fig.1 top). In contrast, the higher HXT energy channels all show highly-correlated fast time structures (Fig.1 bottom), which indicate thick-target emission produced by nonthermal electrons. If we assume that the Lo channel is entirely dominated by thermal emission, $F^{th}_{Lo}(t)$, while the higher channels represent a mixture of thermal and nonthermal emission, e.g. $F_{M1}(t) = F^{th}_{M1}(t) + F^{nth}_{M1}(t)$, we can determine an upper limit to the thermal component of the higher-energy channels using the flux ratio expected from the plasma temperature (cf. Alexander and Metcalf, 1997), e.g. from the ratio of Lo to M1,

$$R_{12}(t) = \frac{F^{th}_{Lo}(t)}{F^{th}_{M1}(t) + F^{nth}_{M1}(t)} \leq \frac{F^{th}_{Lo}(t)}{F^{th}_{M1}(t)} \ . \qquad (1)$$

We find the highest flux ratios at the time t =10:23:54 UT (Fig.1 bottom), with values of Lo/M1=8.3, Lo/M2=63, and Lo/Hi=160. If we divide the flux of the Lo channel by these factors, we obtain lower envelopes to the rapidly-varying, spiky high-energy HXT channels (Fig.1

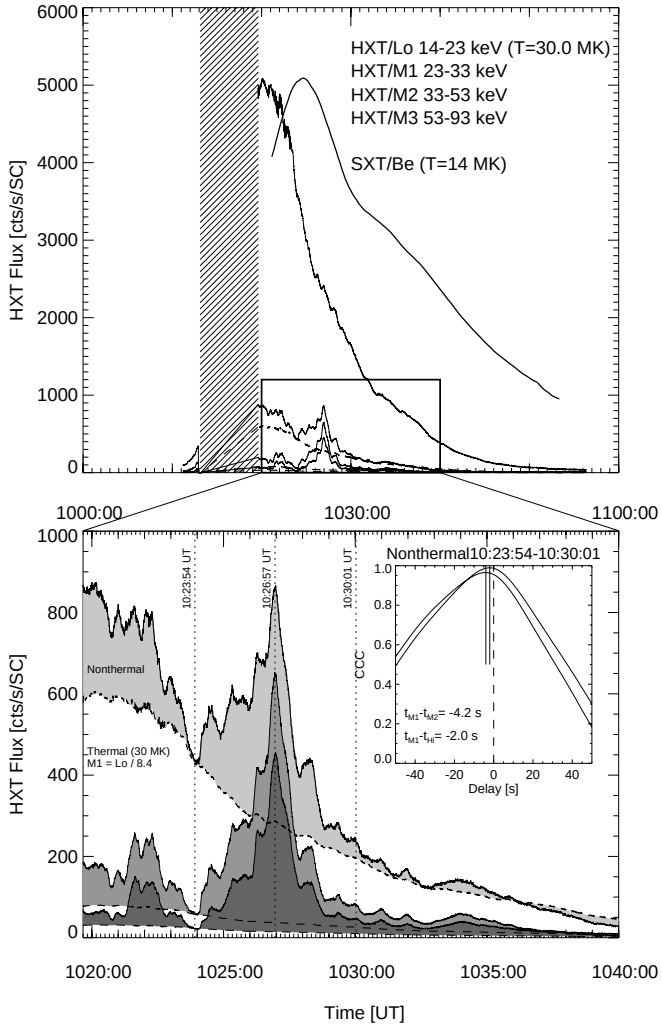

Figure 1. **Top:** Hard X-ray time profiles (in counts per second and subcollimator) from the Yohkoh Hard X-Ray Telescope (HXT), including the 4 energy channels (Lo, M1, M2, Hi), and for comparison a soft X-ray light curve from the Be filter of the Yohkoh Soft X-Ray Telescope (SXT). The hatched area during the rise of the flare demarcates data gaps of the Yohkoh data. A box that encompasses details of the three higher energy channels is shown enlarged in the bottom frame. **Bottom:** The thermal contributions in the three higher HXT channels are estimated from a lower envelope by the softest HXT channel, assumed to be purely thermal. The lower envelopes are found by scaling the HXT/Lo time profile by factors of 1/8.3, 1/63, and 1/160. The insert in the bottom frame shows a cross-correlation of the nonthermal fluxes (with the thermal flux subtracted) during the time interval of 10:23:54-10:30:01 UT, exhibiting time delays of $\Delta t = 4.2$ of channel M2, and $\Delta t = 2.0$ s of channel Hi, with respect to channel M1.

bottom, dashed profiles), which represent upper limits to the thermal contributions in each channel; supposing that the temperature distribution stays constant, and thus the thermal spectrum stays proportional, during the analyzed time interval. The fact that the lower envelopes match not only one valley of the hard X-ray flux at 10:23:54 UT, but all subsequent valleys later on, at 10:32 and 10:33 UT, corroborates our model of a proportional thermal background at multiple times when the intermittent nonthermal emission drops to zero (Sakao et al., 1962). The nonthermal hard X-ray emission is bursty by nature, because of intermittent injection of electrons from the acceleration source towards the chromospheric thick-target. From the flux channel ratio Lo/M1=8.3 we determine a temperature of $T \approx 30$ MK for the thermal flare plasma, see Fig.7 in Alexander and Metcalf (1997). This value represents a true upper limit of the flare plasma temperature. We like to emphasize that this method of determining the flare plasma temperature should be more accurate than previous attempts that assumed that both the Lo and M1 channels are entirely thermal, leading to largely exaggerated temperature values in the range of $T \approx 200$ MK, e.g. (Masuda, 1994).

In Fig.2 we show HXT maps in the 4 energy channels during the three times that mark the evolution from a purely thermal spectrum in Lo and M1 (10:23:54 UT) to maximum nonthermal emission (peaking at 10:26:57 UT) and back to a low nonthermal level (10:30:01 UT) shortly after the main soft X-ray flare peak (see dashed time marks in Fig.1 bottom). The hard X-ray emission (contours in Fig.2) in the Lo channel (14-23 keV) is always centered above the loop tops of the flare arcade seen in soft X-rays (grey scale images in Fig.2), as expected for dominant thermal emission. This confirms our a priori assumption that the Lo channel is almost entirely thermal. The M1 channel (23-33 keV), for which we predict entirely thermal emission at its valley at 10:23:54 UT (Fig.1 bottom), is indeed also centered above the loop top like the Lo channel (Fig.2), which confirms our assumption. At the other times, the M1 channel does not coincide with the thermal emission of the Lo channel, as expected by the significant amounts of nonthermal flux detected in form of bursty pulses above the thermal background (Fig.1 bottom). The higher energy channels M2 and Hi always show dominant footpoint emission (Fig.2), in particular at 10:23:54 UT, when two hard X-ray ribbons are visible (discovered during this flare), supposedly tracing out the two footpoint ribbons of the flare arcade (see also paper by Masuda et al., 2001 in this issue). The observed HXT fluxes of Lo, M1, M2, Hi at 10:23:54 UT are 3600, 433, 58, and 22 cts/s/SC. Based on the thermal spectrum (with $T \approx 30$ MK) constrained by the channel ratio Lo/M1=8.3, we expect flux ratios of Lo/M2=305 and Lo/Hi=650,000, or thermal fluxes of 6000, 433, 11, and 0.0055 cts/s/SC. We conclude

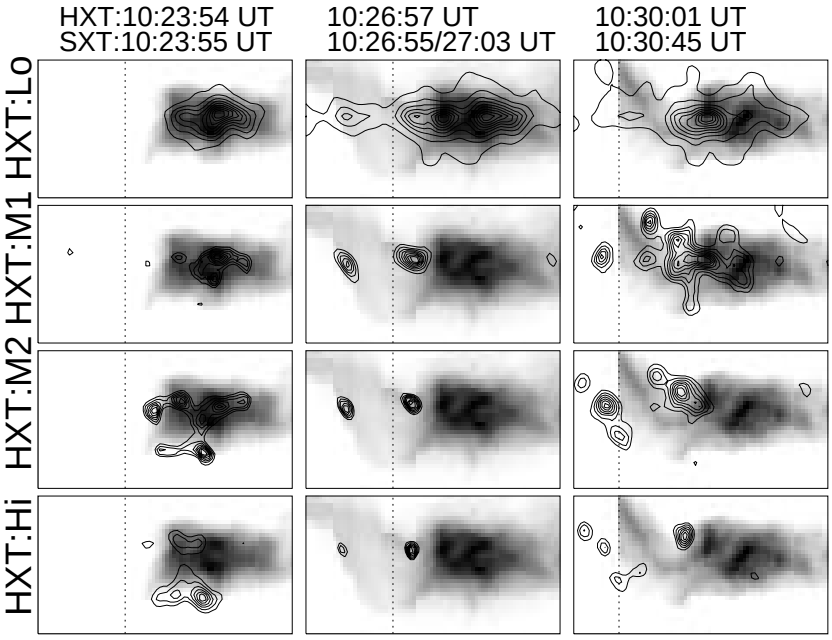

Figure 2. Yohkoh HXT maps (contours) of energy channels (Lo, M1, M2, Hi) at the three times 10:23:54 UT, 10:26:57 UT, 10:30:01 UT indicated (with dotted lines in Fig.1) at begin, peak, and end of a nonthermal episode. The contours are shown in increments of 10%, starting at 10% for Lo, at 20% for M1, at 30% for M2, and at 40% for Hi. The HXT maps are overlayed on SXT/Al12 maps (on logarithmic scale). The second image is a composite of a full-resolution SXT/Al12 and half-resolution SXT/AlMg image. The third SXT image was selected somewhat later to show the location of a developing "spine" in the eastern part above the neutral line. The dotted lines demarcate the field-of-view of the SXT full-resolution frames. The field-of-view is 74×33 pixels (with pixel size 2.455"), i.e. 182"×81" or 132×59 Mm. Note the coincidence of thermal emission in the HXT/Lo channel with SXT emission, as well as in the M1 channel during the first time interval. All other HXT maps are dominated by nonthermal emission, which precedes the thermal SXT emission when electron precipitation is propagating eastward.

therefore that the thermal emission amounts to $11/58 \approx 19\%$ in the M2 channel, and to $0.0055/22 \approx 0.025\%$ in the Hi channel, respectively. The dominant footpoint emission in the M2 channel seen at 10:34:54 UT (Fig.2 left) seems to be consistent with dominant nonthermal emission (81%).

A further piece of information about the nonthermal hard X-ray emission can be extracted from the relative time delays. The cross-correlation of the nonthermal fluxes shows that the higher energies lag behind the lower energy M1 channel, i.e. $\Delta t_{M2} = 4.2$ s and $\Delta t_{Hi} = 2.0$

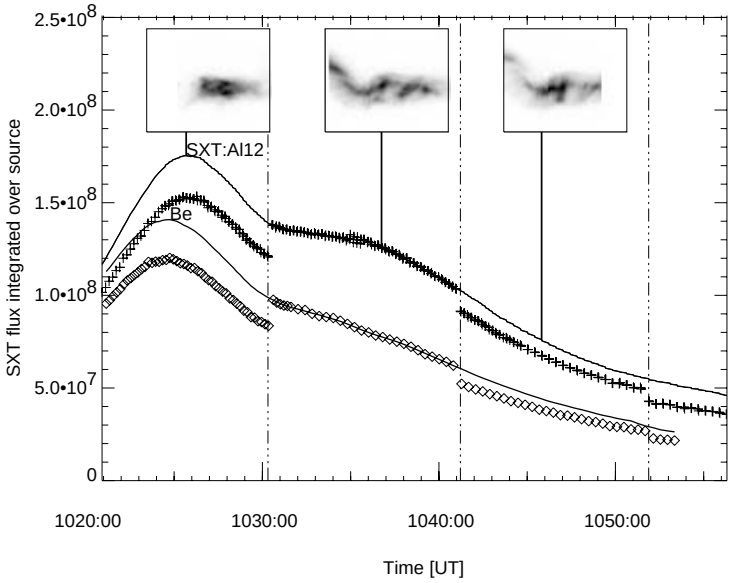

Figure 3. Yohkoh SXT light curves of the Al12 filter (crosses) and Be filter (diamonds). The dash-dotted vertical lines indicate major changes in the spacecraft pointing, which leads to an offset of the total flux integrated over the source, because the field-of-views do not comprise the entire flare arcade. We correct (thick solid lines) for this source truncation by scaling the observed fluxes in all time segments to the middle time segment, where maximum source coverage was obtained. The three inserts show SXT Al12 images (64×64 pixels or 157"×157"), revealing the slightly shifted field-of-views in each of the three time segments.

s (Fig.1 bottom insert). This delay is indicative of electron trapping, because the Coulomb collision times are increasing with higher energies, i.e. $\tau^{coll} \approx 10^8 \; E_{keV}^{3/2}/n_e$ (Aschwanden et al., 1997). The relative delays of 4.2 and 2.0 s between M2 (> 33 keV) or Hi (> 53 keV) with respect to M1 (> 23 keV) are consistent with electron densities in the range of $n_e \approx 2 \times 10^9 - 1.5 \times 10^{10}$ cm^{-3}.

In conclusion, we determined upper limits of $T \lesssim 30$ MK for the flare plasma temperature and $n_e \lesssim 1.5 \times 10^{10}$ cm^{-3} for the plasma density. A higher temperature would exceed the fluxes at the lowest valleys in the M1 and M2 channels, or the Lo channel should contain also a nonthermal component, which is not evident from the lack of spiky time structures. We can therefore firmly assume that the flare plasma evaporated from the chromosphere, after heating by precipitation of nonthermal particles, does not reach a higher initial temperature than $T \lesssim 30$ MK.

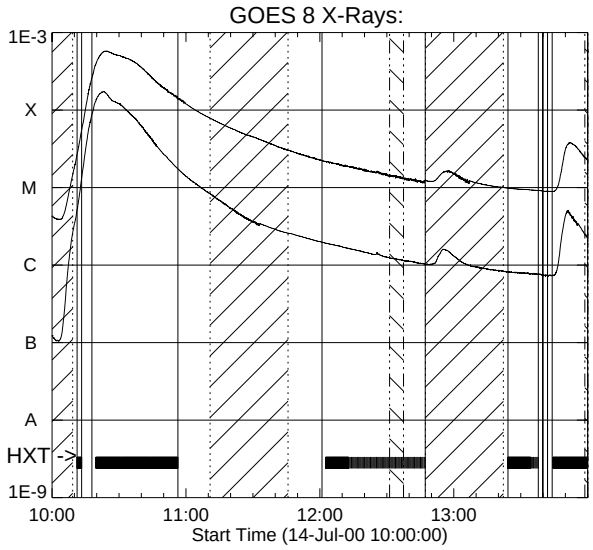

Figure 4. GOES light curves (in units of W m^{-2}), with time intervals of Yohkoh spacecraft night (hatched between dotted lines) and SAA (hatched between dashed-dotted lines). The time intervals with Yohkoh/HXT data are indicated with a thick black bar. Note that the GOES flux does not drop to the preflare level even after 4 hours.

2.2. Yohkoh/SXT Observations

The Yohkoh SXT (Tsuneta et al., 1991) observed the Bastille-Day flare event during the main flare phase of 10:20-11:00 UT. Most of the thin-Aluminium filter (Al1) images were highly saturated, because the high fluxes of this strong flare could not be compensated by sufficiently short exposure times, so that we do not use them for quantitative analysis. We make use of the thick-Aluminium filter (Al12) and the Beryllium filter (Be), for which the total fluxes (integrated over the entire image and normalized for exposure times) are shown in Fig.3. The exposure times varied between 1.4, 3.1, and 6.3 ms for these 64×64 partial frames. There were some major shifts in the pointing around 10:30 UT and 10:41 UT, by amounts of $\approx 20" - 40"$. Because the soft X-ray emission of the entire flare arcade extends beyond the partial frame SXT images, these pointing shifts cause jumps in the total flux. We correct for this offset by scaling the time segments with lesser flux to the middle time segment with the largest flux and most complete coverage of the source location. After this flux correction, we measure a maximum SXT flux of $F_{Al12} = 1.75 \times 10^8$ DN/s for the thick-Aluminium filter, and a maximum flux of $F_{Be} = 1.41 \times 10^8$ DN/s for the Beryllium filter (see Fig.3).

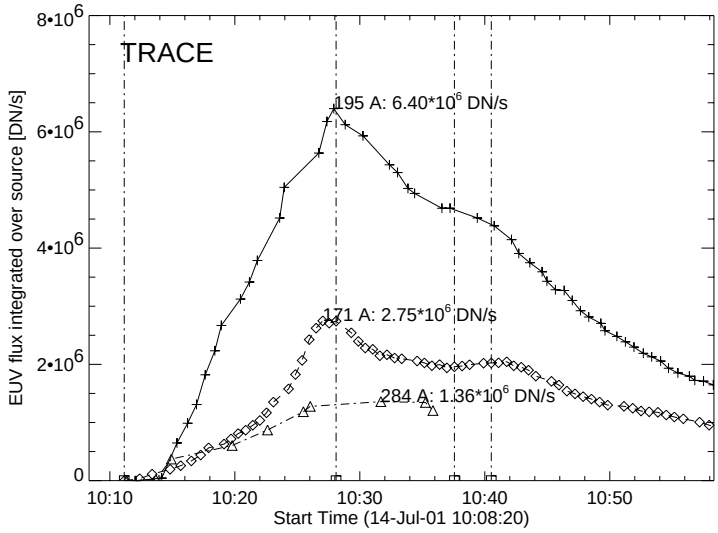

Figure 5. TRACE flux curves integrated over the entire source region, for the 171 Å (diamonds), 195 Å (crosses), and 284 Å (triangles) filter. The peak flux is indicated for each wavelength. The measurements in the 284 Å filter resulted from accidental quadrant shutter mispositionings. The dot-dashed vertical lines mark 4 times for which TRACE 171 Å images are shown in Fig.7.

2.3. GOES Observations

The time profiles of the 0.5-4 Å and 1-8 Å soft X-ray flux from the full Sun as measured by the GOES 8 spacecraft are shown in Fig.4. However, because the preflare levels are 2-3 orders of magnitude lower, the GOES soft X-ray flux is entirely dominated by the Bastille-Day flare. The time resolution of the GOES data is 3.0 s. The GOES low channel (1-8 Å) reaches a maximum flux of $F_{Goes8} = 5.788 \times 10^{-4}$ W m^{-2} at 10:24:24 UT, which defines the flare class as X5.7. The higher GOES channel (0.5-4 Å) reaches a maximum flux of $F_{Goes4} = 1.749 \times 10^{-4}$ W m^{-2} at 10:22:57 UT. Thus the flare emission from the hotter flare plasma peaks earlier.

2.4. TRACE Observations

TRACE (Handy et al., 1999) observed the Bastille-Day flare in 171 Å and 195 Å during the time interval of 2000-Jul-14 10:11:09-10:59:39 UT; see light curves of total flux integrated over the entire source in Fig.5. The quadrant shutter exhibited some irregularities in the filter wheel positioning, so that a number of programmed positions in 195 Å turned out to be in the position for 284 Å , which provides us with an additional light curve in 284 Å (Fig.5). Images taken at intermediate

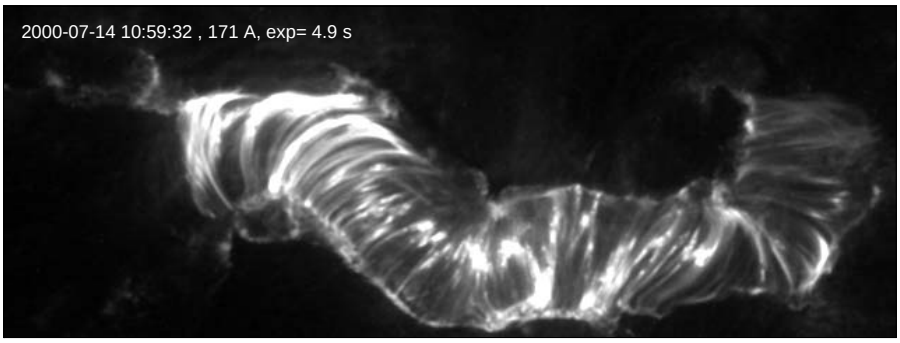

Figure 6. TRACE 171 Å image of the Bastille-Day flare about 40 minutes after the flare peak, when the entire arcade of this double-ribbon flare is illuminated with cooling plasma in the $T = 1 - 2$ MK range, showing a curved sequence of closely-spaced loops with the appearance of a *"slinky"*. The field-of-fiew is 640×256 pixels (with pixel size of 0.5"), which corresponds to 320"×128" or 232×93 Mm.

filter positions have been discarded from the analysis. The exposure times for 171 Å ranged typically from 1.0 to 4.9 s, and for 195 Å from 0.6 to 2.9 s. Some of the 195 Å images show saturation effects, which causes some underestimate of the total EUV flux around the flare peak. The peak times and peak fluxes are listed in Table I.

A typical image of the post-flare arcade is shown in Fig.6. For TRACE movies of the flare evolution see a related paper in this issue (Title et al., 2001). Here we analyze the spatial structure of the flare emission to the extent necessary for modeling of the thermal emission. To enhance the spatial structure we apply a highpass filter, by subtracting a smoothed image (smoothed by 5×5 pixels) from the original images. We show 5 such high-pass filtered 171 Å images in Fig.7. The selected times are indicated in Fig.5 (by dash-dotted vertical lines). The first image (Fig.7 top) shows the very beginning of brightening flare loops in EUV at 10:11:09 UT, which run almost parallel to the neutral line. In the second image at 10:28:06 UT (Fig.7, second from top) we see a highly-sheared, low-lying group of some 25 loops brightening over the western part of the neutral line. In the third image at 10:37:34 UT (Fig.7, third from top), we see less and less sheared arcade loops in the western half of the flare arcade. At the same time a new group of highly-sheared loops start to brighten in the eastern half of the arcade. In the fourth image (Fig.7, fourth from top), an overlying less-sheared group of loops brightens in the eastern part. Finally, at 10:59:32 UT (Fig.7, bottom) we see a higher layer of some 100, almost unsheared loops along the entire arcade.

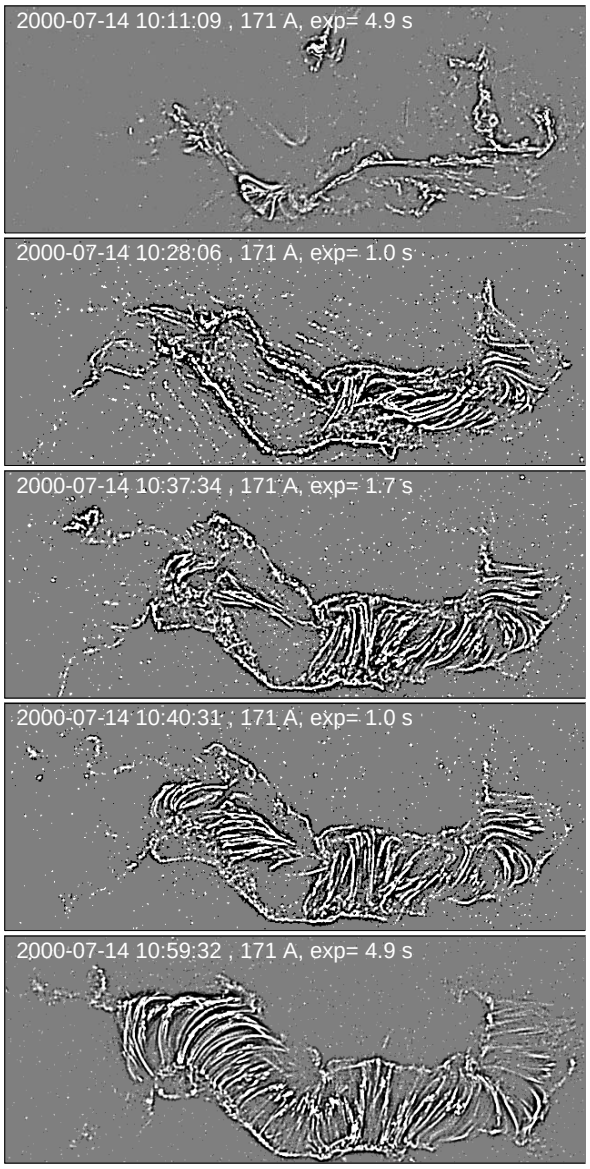

Figure 7. High-pass filtered TRACE 171 Å images of the Bastille-Day flare during 5 time periods of the flare (indicated with vertical lines in Fig.5). The field-of-view is the same as in Fig.6, i.e. 320"×128". The last image is at the same time as Fig.6. Note the sequential brightening of highly-sheared to less-sheared loops, first in the western half, and later in the eastern half of the arcade.

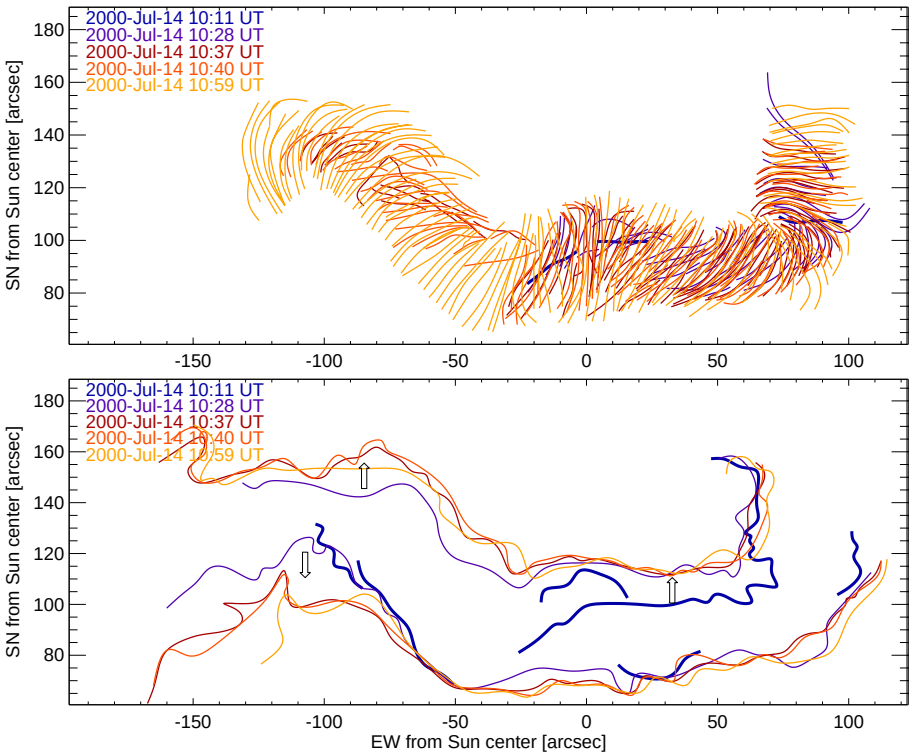

Figure 8. **Top:** Tracings of individual flare loops from the same 5 TRACE 171 Å images shown in Fig.7. The five sets of loops traced at 5 different times are marked with different colors. Note the evolution from highly-sheared to less-sheared loops. **Bottom:** The position of the two flare ribbons traced from TRACE 171 Å images. Note the increasing footpoint separation with time.

In summary, this evolution suggests that the flare arcade is almost solidly filled up with flaring loops, starting from highly-sheared low-lying loops right above the neutral line, up to unsheared high-lying loops in the outer envelope of the arcade. We trace all distinguishable loops in these five images and show their relative position in Fig.8 with different colors, to illustrate the decreasing shear angle with height. The footpoints of the flare loops, which demarcate the so-called flare ribbons, spread initially apart with time, as shown by tracings in Fig.8 bottom. The largest jump in the footpoint separation occurs between the first two times, in the interval of 10:11-10:28 UT.

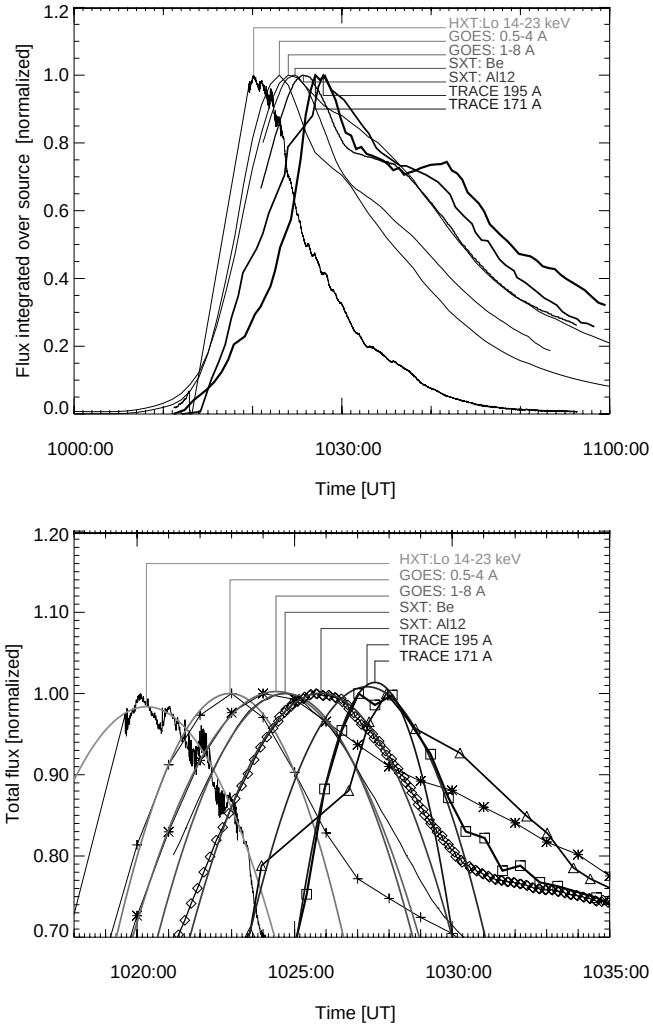

Figure 9. **Top:** Coregistered light curves from Yohkoh/HXT, Yohkoh/SXT, GOES, and TRACE, normalized to unity. **Bottom:** Enlarged portion of the flare peak times, fitted by parabolic curves to determine the mean peak times for each wavelength. Only datapoints in the top 20% of the peak fluxes are considered for the parabolic fits. One single low point of the TRACE 195 datapoints (triangles) before the peak is discarded because of saturation effects. The relative time delays of the peaks are listed in Table I.

Table I. Peak times of total flux in different instruments and wavelengths, and time delays relative to hard X-ray HXT/LO peak.

Instrument Wavelength	Peak time $t_{peak}[MK]$	Time delay t_{delay}
HXT Lo 14-23 keV	10:20:18 UT	0 s
GOES 0.5-4 A	10:22:57 UT	159 s
GOES 1.0-8 A	10:24:24 UT	246 s
SXT Be	10:24:42 UT	264 s
SXT Al12	10:25:50 UT	332 s
TRACE 195 A	10:27:18 UT	420 s
TRACE 171 A	10:27:33 UT	435 s

3. Data Modeling

3.1. Wavelength-Dependent Timing of Flare Peak

We study now the timing of flare emission at different wavelengths, from hard X-rays to soft X-rays and EUV. The coregistered time profiles from Yohkoh/HXT, Yohkoh/SXT, GOES, and TRACE are shown in Fig.9 (top), normalized to unity. All light curves were integrated over the entire field-of-view of each instrument, which generally encompass most of the flaring arcade. The field-of-view is 64x2.45"=157" for Yohkoh SXT full-resolution frames, and 768x0.5"=384" for TRACE images. GOES sees the full Sun, but the flare emission exceeds the background of the remaining Sun by 2-3 orders of magnitude.

The coregistered time profiles show that emission in all wavelengths peak during 10:20-10:28 UT (Fig.9 top). The time profiles in hard X-rays, soft X-rays, and EUV are all similar, except for an increasingly longer decay towards longer wavelengths or lower temperatures. We fit a parabolic curve to the peak at each wavelength (Fig.9 bottom), using the datapoints in the top 20% near the peak flux. We find that there is a well-defined progression of peak times between 10:20 and 10:28 UT, with the hightest energy observations peaking first, starting with hard X-rays, followed by soft X-rays and EUV with decreasing temperature (see Table 1). While most of the wavelengths could be fitted closely by a parabola near the peak of the emission, we note deviations from such a parabola shape for TRACE 195 Å only (Fig.9, bottom), which seems to result from saturation effects in the TRACE images as well as by inaccurate quadrant-shutter positions.

In summary, we learned that the flare peaks are dispersed over about 7 minutes in different wavelengths, with increasing time delay for longer wavelengths or lower temperatures. Because this time delay is likely to be associated with the cooling of the flare plasma temperature, we consider the temperature dependence of the different instruments as next step.

3.2. Differential Emission Measure Modeling

For the flare peak time interval of 10:20-10:28 UT, the major part of the flare arcade is brightest in all wavelengths (Figs.1-9). According to the highest resolution images available (Fig.7), we notice some 25 bright loop structures in the western portion of the flare arcade. We consider now the differential emission measure distribution $dEM(T)/dT$ of this group of brightest loops as a function of temperature. We employ two half gaussian functions as the *ansatz* for an analytical approximation of the DEM distribution:

$$\frac{dEM(T)}{dT} = EM_0 \frac{1}{\sqrt{2\pi}\sigma_{T2}} \exp\left[-\frac{(T-T_0)^2}{2\sigma_{Ti}^2}\right] \begin{cases} \sigma_{T1} & \text{for } T < T_0, \\ \sigma_{T2} & \text{for } T > T_0. \end{cases} \quad (2)$$

(in units of cm^{-3} K^{-1}), with the total emission measure defined by

$$EM_{tot} = \int_0^\infty \frac{dEM(T)}{dT} dT \ . \quad (3)$$

(in units of cm^{-3}). For $\sigma_{T1} = \sigma_{T2} \ll T_0$, this normalization yields $EM_{tot} = EM_0$. The different instruments used here have a temperature-dependent response function $R(T)$ that is characterized by the flux units that are measured per unit emission measure $dEM(T)$ at temperature T,

$$R_{Instr}(T) = \frac{dF_{Instr}(T)}{dEM(T)} \ . \quad (4)$$

The corresponding response functions $R_{Instr}(T)$ are shown in Fig.10 (middle panel), normalized to unity at the maximum in the temperature range of $T = 0.5 - 50$ MK. All response functions can numerically be obtained from the *Solar SoftWare (SSW)* (Freeland and Handy, 1998) using the *Interactive Data Language (IDL)*, i.e. the functions and prcedures *TRACE_RESP.PRO*, *SXT_FLUX.PRO*, *HXT_T6_RESP0.PRO*, and *MAKE_GOES_RESP.PRO*.

Each instrument sees only a certain temperature slice of the total differential emission measure distribution $dEM(T)/dT$ (Eq.2). We define the temperature contribution function $dF(T)/dT$ of the flux F by a convolution of the differential emission measure distribution

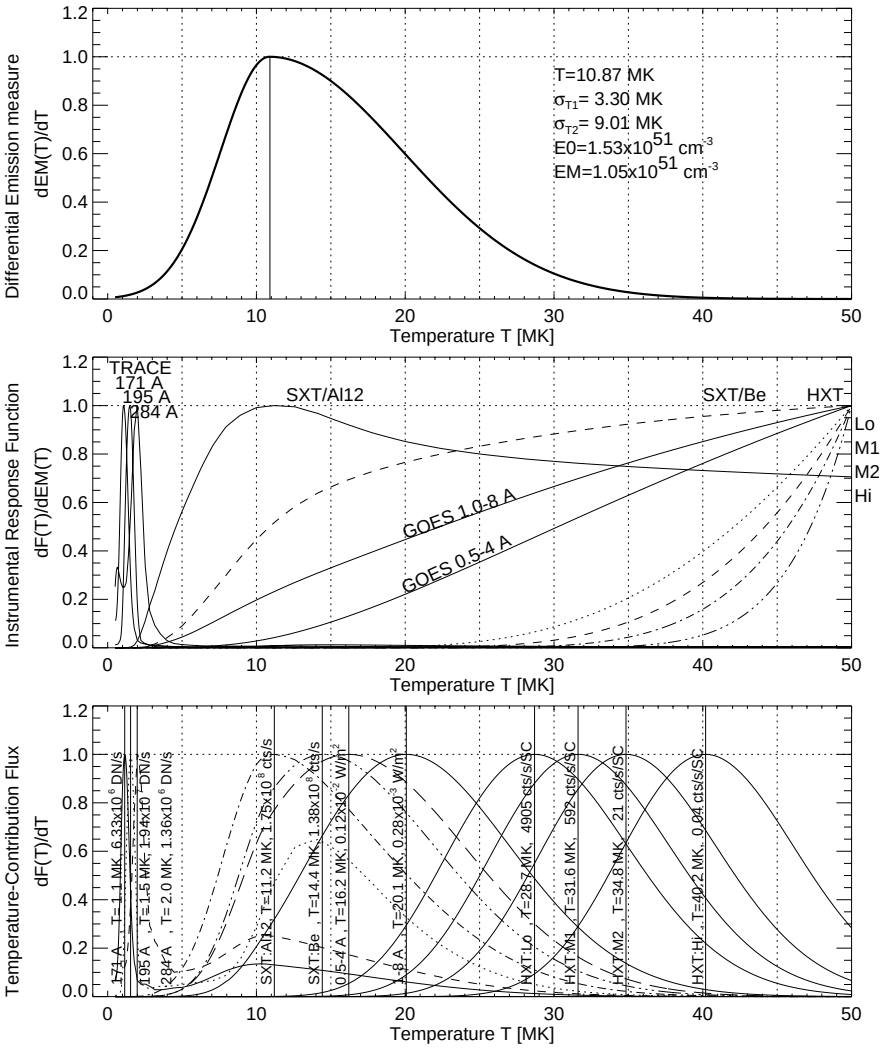

Figure 10. **Top:** Best-fit model of differential emission measure distribution during the flare peak that is consistent with the detected fluxes observed by TRACE, GOES, and YOHKOH. **Middle:** Instrumental response functions, normalized to unity at the maximum in the temperature range of $T = 0.1 - 50$ MK. **Bottom:** Temperature contribution functions of the fluxes $dF_{Instr}(T)/dT$ detected by each instrument filter, normalized to unity. The absolute flux values and peak temperatures are labeled for each instrument filter, and are also listed in Table II.

$dEM(T)/dT$ with the instrumental response functions $R_{Instr}(T)$ for each instrument, i.e.

$$\frac{dF_{Instr}(T)}{dT} = \frac{dF_{Instr}(T)}{dEM(T)} \otimes \frac{dEM(T)}{dT} = R_{Instr}(T) \otimes \frac{dEM(T)}{dT} \ . \quad (5)$$

These contribution functions $dF_{Instr}(T)/dT$ are shown for each instrument in Fig.10 (bottom frame). The total flux F_{Instr} recorded by each instrument is given by the integral over the entire sensitive temperature range,

$$F_{Instr} = \int \frac{dF_{Instr}(T)}{dT} dT = \int R_{Instr}(T) \otimes \frac{dEM(T)}{dT} dT \ . \quad (6)$$

The determination of the unknown differential emission measure distribution $dEM(T)/dT$, parametrized by two half-gaussians with four free parameters ($T_0, \sigma_{T1}, \sigma_{T2}, E_0$; Eq.2), can now simply be achieved by forward-fitting to the observed fluxes, until a minimum of the relative differences

$$\Delta F = \sum_{Instr} \frac{(F_{Instr}^{model} - F_{Instr}^{obs})}{F_{Instr}^{model}} \quad (7)$$

is obtained. We cannot use a χ^2-criterion, because the relative uncertainties of the inter-calibration between the instruments, which is much larger than the photon statistics here, is not known. The observed total fluxes F_{Instr}^{obs} and the best-fit values F_{Instr}^{model} are shown in Table II. We find a best fit for the following parameters of the gaussian differential emission measure distribution $dEM(T)/dT$: a mean temperature of $T_0 = 10.87$ MK, gaussian widths of $\sigma_{T1} = 3.30$ MK and $\sigma_{T2} = 9.01$ MK, and an emission measure factor of $EM_0 = 1.53 \times 10^{51}$ cm^{-3}, yielding a total emission measure of $EM_{tot} = 1.05 \times 10^{51}$ cm^{-3}. The resulting DEM is shown in Fig.10 (top), indicating that the bulk of the flare plasma has a temperature range of $T \approx 1 - 35$ MK.

The corresponding temperature contribution functions $dF_{Instr}(T)/dT$ are shown in Fig.10 (bottom), which represent the relative plasma contributions at different temperatures that make up the detected flux for a given instrument. These distributions indicate that the TRACE 171, 195, and 284 filters are most sensitive to plasma temperatures of $T = 1.0, 1.5$, and 2.0 MK respectively, Yohkoh/Al12 and Be filters to temperatures of $T = 11.2$ and 14.4 MK, the GOES 0.5-4 Å and 1-8 Å channels to $T = 16.2$ and 20.1 MK, and the Yohkoh/HXT Lo and M1 channels to $T = 28.7$ and 31.6 MK, respectively, for this particular differential emission measure distribution $dEM(T)/dT$. Note also that the thermal fluxes predicted for HXT/M2 and Hi are significantly below the observed values (Table II), confirming that those channels are dominated by nonthermal fluxes.

Table II. Best-fit parameters of differential emission measure distribution $dEM(T)/dT$ model with $T_0 = 10.87$ MK, $\sigma_{T1} = 3.30$ MK, $\sigma_{T2} = 9.01$ MK, and $EM_{tot} = 1.53 \times 10^{51}$ cm^{-3}.

Instrument Wavelength	Temperature T_{peak}	Model flux F_{model}	Observed flux F_{obs}	Ratio F_{model}/F_{obs}
HXT Hi 53-93 keV	40.2 MK	0.04 cts/s	<28 cts/s	–
HXT M2 33-53 keV	34.8 MK	21 cts/s	<78 cts/s	–
HXT M1 23-33 keV	31.6 MK	592 cts/s	594 cts/s	0.997
HXT Lo 14-23 keV	28.7 MK	4905 cts/s	5090 cts/s	0.964
GOES 1.0-8 A	20.1 MK	0.28×10^{-3} W/m^2	0.17×10^{-3} W/m^2	1.620
GOES 0.5-4 A	16.2 MK	1.20×10^{-3} W/m^2	0.58×10^{-3} W/m^2	2.145
SXT Be	14.4 MK	1.38×10^{8} cts/s	1.40×10^{8} cts/s	0.985
SXT Al12	11.2 MK	1.75×10^{8} cts/s	1.75×10^{8} cts/s	1.000
TRACE 284 A	2.0 MK	1.36×10^{6} DN/s	1.36×10^{6} DN/s	0.999
TRACE 195 A	1.5 MK	1.94×10^{7} DN/s	6.46×10^{6} DN/s	3.009
TRACE 171 A	1.0 MK	6.33×10^{6} DN/s	2.75×10^{6} DN/s	2.302

3.3. Inter-Calibration of Instruments

The ratios of the predicted fluxes to the observed fluxes from the best-fit values of the $dEM(T)/dT$ distribution (Table II) provide us some hints about the inter-calibration accuracy of the different instruments. Using the subset of 4 Yohkoh instruments, i.e. HXT:Lo,M1, and SXT:Al12,Be, we find a solution for the $dEM(T)/dT$ that predicts the total fluxes within $\lesssim 2\%$ of the observed fluxes. If we use the Yohkoh instruments as standard calibration, we find that the TRACE calibration yields a fully consistent flux at 284 Å (within $< 1\%$), but too high fluxes at 195 Å (by a factor of 3.0) and 171 Å (by a factor of 2.3). Part of the discrepancy between Yohkoh and TRACE calibration is the different assumptions about elemental abundances. We used the Grevesse-Rothenflug response function for TRACE, which makes use of the Meyer (1985) chromospheric abundances, which are more consistent with the Yohkoh calibration than the coronal abundances by Feldman (1992), which would result in an even larger discrepancy (see Appendix A in Aschwanden et al. 2000). Another reason for the relatively high predicted TRACE fluxes is the degradation of the lumogen, estimated to be of order $\lesssim 50\%$ at the time of the Bastille-Day flare, which is not accounted for in the TRACE response function.

The GOES instruments are found to be too high relative to Yohkoh too, both the 0.5-4 Å (by a factor 2.1) and the 1-8 Å (by a factor 1.6) channel, probably also because different elemental abundances have

been used in the calculation of the response functions. Nevertheless, it can be said that the calibrations of the 9 instrument channels agree within a factor of $\lesssim 2$ for the best DEM solution. This inter-calibration result is based on several assumptions, such as (1) the existence of a smooth (e.g. piece-wise gaussian) $dEM(T)/dT$ distribution, (2) constant $dEM(T,t)/dT$ during the analyzed time interval around the flare peak (10:20-10:28 UT), and (3) no problems with measurements of the total flux (saturation, field-of-view, etc.). However, because the contribution functions $dF(T)/dT$ are substantially overlapping (Fig.10 bottom), the results of the relative inter-calibration ratios should be quite robust.

3.4. Cooling Function of Flare Loops

The spatial analysis in Section 2.4 has shown that this flare arcade consists of a number of some hundred individual loops. As a first approximation we assume that all these loops are subject to a similar evolution, i.e. rapid filling with heated chromospheric plasma and subsequent cooling of the flare plasma from a peak temperature of ≈ 30 MK down to $\lesssim 1$ MK. If we assume that all loops are approximately heated to the same peak temperature and cool down with a similar time evolution, we can determine the cooling function $T(t)$ of a single loop just from the statistical average of all simultaneously brightening loops, according to the superposition principle. In essence, if we add up the flux profiles $F(T[t-t_1])$ of many loops with arbitrary relative time phases of their heating t_1, the superposition $\Sigma F(T[t-t_1])$ will exhibit in first order the same temperature-dependent time delays $t(T)$ as a single loop. Based on this equivalence, we infer that the observed temperature-dependent delays $\Delta t(T)$ (listed in Table I according to wavelengths) as function of the wavelength-dependent peak temperatures T_{peak} of the contribution functions F_{obs} (given in Table II) reflect the intrinsic cooling function $T(t)$ of the average single loop. Thus, relating the time delays Δt given in Table I to the temperature peaks listed in Table II, we infer a cooling function $T(t)$ as shown in Fig.11 (top left), indicating a monotonic decrease of the temperature from $T \approx 30$ MK down to $T \approx 1$ MK over a time interval of about 7 minutes.

Let us understand the physical nature of this observed cooling function $T(t)$. Because the temperature T_1 and temperature gradients $dT(t = t_1)/ds$ of a loop heated at time $t = t_1$ are initially highest, it is expected that conductive cooling dominates initially. Neglecting all other terms in the hydrodynamic energy equation, the enthalpy loss $dE_{ent}(t)/dt$ is

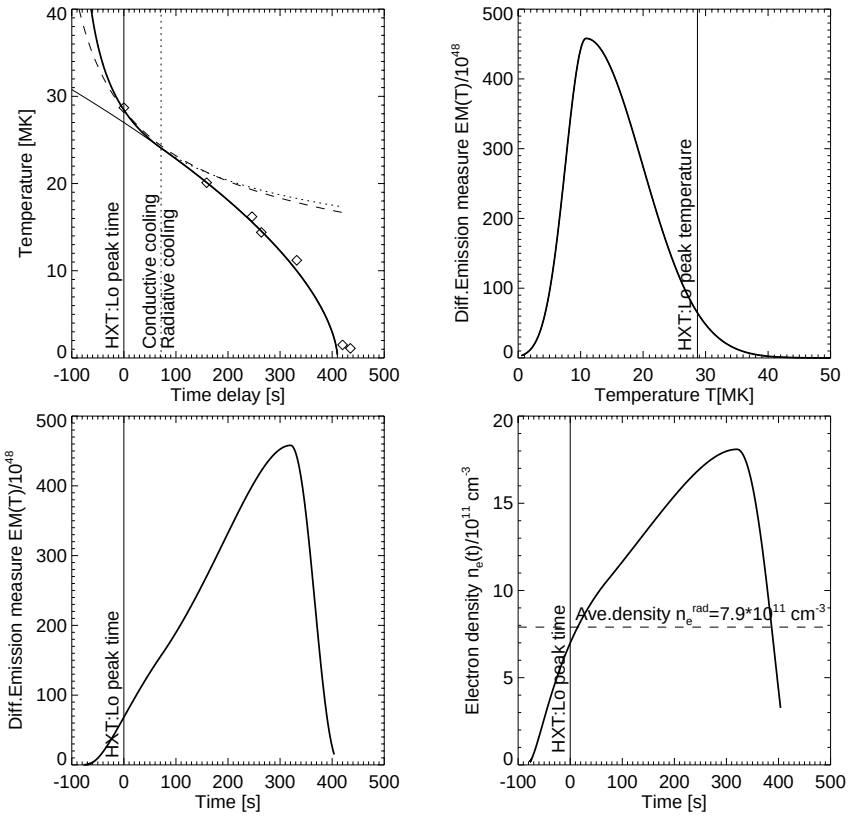

Figure 11. Evolution of the temperature $T(t)$, the differential emission measure $EM(t)$, and electron density $n_e(t)$ of an average flare loop during the flare peak phase. Theoretical models of the cooling function $T(t)$ include conductive cooling models, (Antiochos and Sturrock 1978, dotted line, Eq.12; Culhane et al. 1994, dashed line, Eq.9), and the radiative cooling model (solid curves, Eqs.14, 19), fitting the observed peak time delays $t_{peak}(T)$ (diamonds).

then mainly balanced by the thermal conduction loss rate,

$$\frac{d}{dt}E_{ent}(t) = \frac{d}{dt}[3n_e(t)k_BT(t)] = \frac{d}{ds}\left(\kappa T^{5/2}\frac{dT(t)}{ds}\right) \approx -\frac{2}{7}\kappa\frac{T(t)^{7/2}}{L^2} \tag{8}$$

with κ the Spitzer thermal conductivity and L the loop half length. This differential equation (Eq.8) can be directly integrated, if we apply the mean-value theorem to the time dependence of the density $n_e(t)$, by replacing it by the mean value $< n_e >$ outside of the integral. The

resulting temperature evolution is then

$$T(t) = T_1 \left(1 + \frac{(t - t_1)}{\tau_{cond}}\right)^{-2/5} \tag{9}$$

with a "conduction time scale" τ_{cond} defined by

$$\tau_{cond} = \frac{21}{5} \frac{< n_e > k_B L^2}{\kappa T_1^{5/2}} \tag{10}$$

This solution was used in (Culhane et al., 1994) to fit the cooling of a flare plasma from $T_1 = 22$ MK down to 12 MK. Antiochos and Sturrock (1978) derived a more general cooling function by including the flow velocities v in the hydrodynamic energy equation

$$-\frac{5}{2}\frac{p}{n_e}\left(\frac{\partial n_e}{\partial t} + v\frac{\partial n_e}{\partial s}\right) = \frac{\partial}{\partial s}(\kappa \frac{\partial T}{\partial s}) \tag{11}$$

Solving this hydrodynamic equation they find a slightly different solution for the cooling curve:

$$T(t) = T_1 \left(1 + \frac{(t - t_1)}{\tau'_{cond}}\right)^{-2/7} \tag{12}$$

We fit both solutions from Culhane et al. (1994) and Antiochos and Sturrock (1978) to our measured cooling curve $T(t)$, in the initial time interval at the highest temperature (Fig.11, top left), but do not find agreement for the later time intervals, and thus conclude that *the later cooling phase of this flare is not dominated by conductive cooling.*

Alternatively, we consider dominant radiative cooling. Equating the enthalpy loss $dE_{enth}(T[t])/dt$ to the radiative cooling rate,

$$\frac{d}{dt}[3n_e(t)k_B T(t)] = -n_e(t)^2 \Lambda(T[t]) \approx -n_e(t)^2 \Lambda_0 T(t)^{-2/3} \tag{13}$$

according to the piece-wise power-law approximation of the radiative loss function $\Lambda(T)$ by Rosner et al. (1978), and applying again the mean-value theorem for the time-dependence of the density $n_e(t)$, we can integrate Eq.(13) analytically and find the solution

$$T(t) = T_1 \left[1 - \frac{(t - t_1)}{\tau_{rad}}\right]^{3/5} \qquad t_1 < t < \tau_{rad} \tag{14}$$

with a "radiative cooling time" τ_{rad} defined by

$$\tau_{rad} = \frac{9 k_B T_1^{5/3}}{5 < n_e > \Lambda_0} \tag{15}$$

We fit this radiative cooling function to the data in Fig.11 and find a surprisingly good fit, except for the first data point. The best-fit parameters are $T_1 = 27$ MK and $\tau_{rad} = 420$ s, yielding a mean density of

$$< n_e >_{rad} = \frac{9 k_B T_1^{5/3}}{5 \Lambda_0 \tau_{rad}} \tag{16}$$

with a value of $< n_e >= 7.9 \times 10^{11}$ cm^{-3}. Therefore we conclude *that the later phase of this flare is dominated by radiative cooling.*

For an anlytical model we synthesize the conductive cooling phase ($T^{cond}(t)$, Eq.12) in the initial phase of loop heating with the dominant radiative cooling ($T^{rad}(t)$, Eq.14) in the later phase. We join the two analytical solutions smoothly together at time t_2, where we require a steady function, $T^{cond}(t = t_2) = T^{rad}(t = t_2)$, and a smooth derivative, $dT^{cond}(t = t_2)/dt = dT^{rad}(t = t_2)/dt$. These two boundary conditions yield with Eqs.12 and 14 the transition time t_2,

$$(t_2 - t_1) = \frac{10 \tau_{rad} - 21 \tau'_{cond}}{31} \tag{17}$$

and initial temperature T_2 of the conductive phase,

$$T_2 = T_1 \frac{(1 - t_2/\tau_{rad})^{3/5}}{(1 + t_2/\tau'_{cond})^{-2/7}} \ . \tag{18}$$

The synthesized cooling model $T(t)$ reads then (for a reference time t_1),

$$T(t) = \begin{cases} T_2 (1 + \frac{(t-t_1)}{\tau'_{cond}})^{-2/7} & \text{for } t_1 < t < t_2, \\ \\ T_1 (1 - \frac{(t-t_1)}{\tau_{rad}})^{3/5} & \text{for } t_2 < t < \tau_{rad}. \end{cases} \tag{19}$$

We find an initial temperature of $T_2 = 28.4$ Mm (at time t_1) and a transition time of $t_2 - t_1 = 71$ s, with a total cooling time of $\tau_{rad} = 420$ s.

3.5. Emission Measure Evolution of Flare Loops

Assuming a rapid heating phase with a monotonic cooling function $T(t)$ (Fig.11 top left), combined with the (instrument-independent) differential emission measure distribution $dEM(T)/dT$ (Fig.11 top right), we can infer the average evolution of the differential emission measure distribution as function of time, by substituting the time dependence $T(t)$ into the differential emission measure distribution, i.e. $dEM(t)/dT = dEM(T[t])/dT$ (Fig.11 bottom right). This yields a differential emission measure that starts to increase (with an initial temperature of $T \gtrsim 30$

MK) up to a maximum after t=350 s (at a temperature of $T \approx 10.0$ MK), and then decreases rapidly until t=420 s, when it is cooled down to $T \approx 1$ MK. The cooled plasma may undergo catastrophic cooling subject to thermal instabilities later on, when it reaches the maximum of the radiative loss function at $T \lesssim 0.5$ MK (not measured here). This time evolution is fully constrained by the observed time delays $\Delta t(T)$ (Table 1 and Fig.9) and the inferred $dEM(T)/dT$ (Fig.10) in our model.

Associating the gaussian-like differential emission measure distribution $dEM(T)/dT$ of the flare with the temperature evolution of a single loop, $EM_{loop}(T)$, we can substitute the temperature evolution $T(t)$ from our synthesized cooling model (Eq.19) and obtain its time evolution,

$$EM_{loop}(t) = EM_0 \exp\left[- \frac{(T(t) - T_0)^2}{2\sigma_{Ti}^2} \right] \begin{cases} \sigma_{T1} & \text{for } T < T_0, \\ \sigma_{T2} & \text{for } T > T_0. \end{cases} \tag{20}$$

Using the standard relation of the total emission measure for optically-thin radiation, we can then also determine the evolution of the loop density $n_e(t)$,

$$n_{e,loop}(t) = \sqrt{\frac{EM_{loop}(t)}{V_{loop}}} \tag{21}$$

Next we have to estimate the volume V_{loop} of an average loop. Based on the total length of the arcade $L \approx 180$ Mm and a loop count of $N_{loops} \approx 100$ (Figs.6,7) along the arcade we infer a mean separation of 1.8 Mm, and thus an upper limit of $r \leq 0.9$ Mm for the cylindrical radius of each loop. The footpoint separation of the arcade amounts to $2R \approx 35$ Mm. The volume of a semi-circular loop is thus

$$V_{loop} = \pi R \times \pi r^2 = 1.40 \times 10^{26}\ cm^3 \tag{22}$$

The average density of a flare loop can then be expressed as time average over its cooling phase period $0 < t < \tau_{rad}$,

$$< n_{e,loop}(t) >= \frac{1}{\tau_{rad}} \int_0^{\tau_{rad}} \sqrt{\frac{EM_{loop}(t)}{V_{loop}}} dt \ . \tag{23}$$

This time-averaged density $< n_{e,loop}(t) >$ of a single loop should be consistent with the average density $< n_e >_{rad}$ (Eq.16) we infer from the radiative cooling time (Eq.15). We use this constraint to define the emission measure of a single loop, i.e.

$$< n_{e,loop}(t) >=< n_e >_{rad} \ . \tag{24}$$

This requirement defines now the emission measure constant EM_0 in Eq.20, i.e.

$$EM_0 =< n_e >^2_{rad} V_{loop} \frac{\tau_{rad}}{\sqrt{\int_0^{\tau_{rad}} \exp\left[-(T(t)-T_0)^2/2\sigma^2_{Ti}\right] dt}} \tag{25}$$

3.6. Flare Plasma Filling Factor

The fraction of the flare volume that is filled by heated plasma is called the filling factor. For this purpose we have to estimate the volume V_{arcade} from the total length of the arcade $L \approx 180$ Mm and the footpoint separation of the arcade, $2R \approx 35$ Mm. The total volume of a semi-cylindric arcade is then

$$V_{arcade} = \frac{\pi R^2 L}{2} \approx 8.66 \times 10^{28}\ cm^3 \tag{26}$$

We can now define two different filling factors: (1) an "instantaneous" filling factor $q_{fill}(t)$ that characterizes what fraction of the arcade is filled with hot plasma at a given time t, which varies as function of time, or (2) a time-integrated filling factor Q_{fill}, which describes what fraction of the flare arcade that was ever filled with heated plasma. The latter fraction can be estimated just by the geometric ratio of all flare loops (even if they don't shine all at the same time) to the total arcade volume. From the loop counts in Figs.6-8 we estimate the total number of flare loops to $N_{loop} \approx 100$, which yields a time-integrated filling factor of

$$Q_{fill} = \frac{N_{loop} V_{loop}}{V_{arcade}} \approx 0.16\ . \tag{27}$$

The instantaneous filling factor $q_{fill}(t)$, say at the time of the flare peak $t = t_P$, has to be determined from the instantaneous number of "bright loops", specified by the ratio of the total emission measure at the flare peak EM_{tot} to the total emission measure per loop,

$$n_{loop}(t = t_{peak}) = \frac{EM_{tot}(t)}{EM_{tot,loop}(t)} \approx 23 \tag{28}$$

for which we find a number of 23 loops (see also fit in Fig.12). This is in good agreement with the number counts of loops at the flare peak time $t_{peak} \approx$ 10:28 UT (second frame from top in Fig.12). The instantaneous filling factor is thus correspondingly,

$$q_{fill}(t = t_{peak}) = \frac{n_{loop}(t = t_{peak}) V_{loop}}{V_{arcade}} \approx 0.037 \tag{29}$$

The more important quantity is the time-integrated filling factor $Q_{fill} \approx 0.16$, which states that about a fraction of 1/6 of the flare arcade was heated at one time, which represents the arcade volume that was accessible to chromospheric evaporation, or an upper limit of the chromospheric arcade area that became bombarded by precipitating particles in the thick-target model.

3.7. Thermal Energy Budget of Flare

With the knowledge of the volume filling factor, the mean density and temperature we can determine a fairly accurate number of the total thermal energy of the flare, i.e.

$$E_{thermal} = 3 < n_e > k_B < T_e > V_{arcade} Q_{fill} \approx 4.9 \times 10^{31} \text{ erg} \quad (30)$$

using the mean density $< n_e >=< n_e >_{rad}= 7.9 \times 10^{11}$ cm^{-3}, the mean temperature $< T >= T_0 = 10.87$ MK, the flare arcade volume $V_{arcade} = 8.66 \times 10^{28}$ cm^3, and a filling factor of $Q_{fill} = 0.16$. Although we dont quantify the energy budget of kinetic and nonthermal energies, which may double the total energy input of the flare to $E_{flare} \approx 10^{32}$ erg, this event it clearly one of the largest observed flares. The total magnetic energy for this flare, contained in a magnetic flux rope at the location of the flare arcade, was estimated to $E_{magn} = 1.6 \times 10^{32}$ erg from non-linear force-free magnetic field extrapolations (Yan, 2001).

3.8. Light-Curve Modeling of the Cooling Flare Plasma

We model now the light curves observed in 9 different wavelength channels based on our analytical loop cooling function $T(t)$ and DEM distribution $dEM(T[t])/dT$. This allows us to refine the physical parameters of the loop cooling function $T(t)$ and to provide a consistency test, whether the predicted peak delays $t_{peak}(T)$, based of the analytical cooling function, agree with the observed multi-wavelength peak delays t_{obs}^{Instr}, after convolution with the temperature-dependent instrumental response functions $R^{Instr}(T)$.

Because the total flux $F(t)$ is time-varying in each wavelength, we need to introduce a time-varying function in a temporal flare model, even if we assume an identical cooling function $T(t)$ for each loop. The largest variation is introduced by the rate of flare loops that become activated by filling of upflowing, heated chromospheric plasma. The rate of activated loops $N(t)$ increases during the rise time before a flare peak and decreases during the decay phase, so we may use a gaussian function to characterize this variation of the loop rate $N(t)$ around a flare peak. For more complex time profiles, a number of flare peaks may

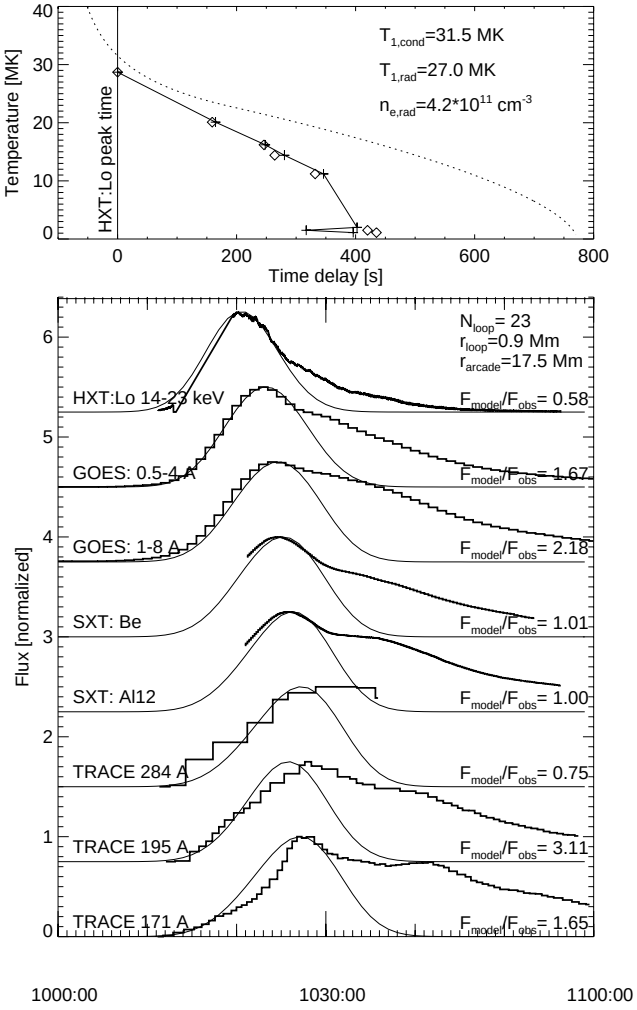

Figure 12. Modeling of the main peak of light curves for 8 different wavelength channels (from 4 instruments) by forward-fitting of our analytical model. The analytical model is based on the cooling function $T(t)$ (dotted curve in top frame) constrained by the observed time delays of the time profile peaks (diamonds in top frame). The resulting time delays of the time profile peaks from the analytical model are shown with a solid line (and crosses) in the top frame. The observed time profiles are shown in the bottom frame (thick histograms), along with the predicted time profiles near the main peak from the analytical model (thin gaussian curves), both normalized to unity and shifted by increments for clarity. The instrumental calibration mismatch factors are shown on the right side, using Yohkoh/SXT Al12 as reference ($F_{model}/F_{obs} = 1.00$). The resulting time delays of the time profile peaks from the analytical model are shown with a solid line (and crosses) in the top frame. The best-fit parameters of $T_{1,cond}, T_{1,rad}, n_{e,rad}$, and N_{loop} are indicated also.

be represented just by a superposition of gaussians with different peak times, i.e.

$$N(t) = \sum_{i_p=1}^{N_{peaks}} N_{i_p} \exp\left[-\frac{(t-t_{p_i})^2}{2\sigma_{p_i}^2}\right] \ , \tag{31}$$

In our Bastille-Day flare, there is indication of a least two major peaks in the flare time profiles, and thus in the rate of activated loops $N(t)$. We concentrate on the first main peak at $t_{P1} \approx$10:20 UT for a group of loops in the western part of the flare arcade, for which we determined the average cooling function $T(t)$. The gaussian width is about $\sigma_{P1} \approx 4$ min, and the total number of involved loops amounts to $N(t) \approx 25$, as counted from the loop tracings in Fig.7.

The emission measure of a specific loop $EM_{loop}(T[t])$ at time t depends on its heating time $t_{1,loop}$ and temperature evolution $T(t - t_{1,loop})$,

$$EM_{loop}(T[t]) = n_e^2(t[T] - t_{1,loop})V_{loop} \tag{32}$$

which requires an inversion of the synthesized cooling funcion $T(t)$ (Eq.19), i.e.

$$t(T) = \begin{cases} t_{1,loop} - \tau'_{cond}[(T/T_2)^{-7/2} - 1] & \text{for } T > T_{CR}, \\ t_{1,loop} - \tau_{rad}[1 - (T/T_1)^{5/3}] & \text{for } T < T_{CR}. \end{cases} \tag{33}$$

where T_{CR} represents the temperature at the transition from conductive to radiative cooling, $T_{CR} = T(t = t_2)$ (with t_2 defined in Eq.17). The flux measured $F_{Instr}(t)$ by an instrument as function of time can then be simulated by convolving the emission measure distribution $EM_{loop}(T)$ with the instrumental response function $R_{Instr}(T)$, summing in each temperature interval $T \mapsto T + dT$ over all loops that contribute to this temperature, based on their heating time $t(T)$ (Eq.33), which is defined by the number of activated loops in the corresponding time interval,

$$N(T \mapsto T + dT) = \int_{t(T)}^{t(T+dT)} N(t)dt \tag{34}$$

This way we obtain the flux time profiles $F_{Instr}(t)$ for each instrument

$$F_{Instr}(t) \int_0^\infty R_{Instr}(T)N(T \mapsto T + dT)EM_{loop}(T)\ dT \tag{35}$$

These simulated time profiles are shown in Fig.12, along with the observed time profiles of our 9 different instrument wavelengths. We refine the fits by optimizing the predicted peak time delays of the simulated time profiles with the observed peak delays (Fig.12 top) and

Table III. Numerical values of physical parameters obtained from direct inversion of the observed peak time delays, equivalent to a single flare loop with a δ-function of the flux $f(t)$, and best-fit parameters obtained by forward-fitting with a gaussian time profile of the flux $f(t)$ to the observed time profiles (Fig.12).

Physical Parameter	Direct Inversion from observations	Best-fit Parameters from Forward-Fitting
Arcade length L	180 Mm	
Arcade radius R	17.5 Mm	
Arcade volume V	8.66×10^{28} cm^{-3}	
Loop radius	0.9 Mm	
Loop volume	1.40×10^{26} cm^{3}	
Number of loops	23	
Arcade filling factor Q_{fill}	0.16	
DEM peak temperature T_0	10.87 MK	
DEM guassian widths σ_{Ti}	3.30, 9.01 MK	
DEM constant EM_0	1.53×10^{51} cm^{-3}	
Total emission measure EM_{tot}	1.05×10^{51} cm^{-3}	
Loop Emission measure EM_{loop}	4.57×10^{49} cm^{-3}	
Temperature constants T_2, T_1	28.4 MK, 27 MK	31.5 MK, 27 MK
Transition temperature T_2	24.1 MK	22.8 MK
Transition time t_2	71 s	188 s
Conductive time scale t_{cond}	90 s	
Radiative cooling time t_{rad}	420 s	780 s
Average Electron density n_e	7.9×10^{11} cm^{-3}	4.2×10^{11} cm^{-3}
Total thermal energy $E_{thermal}$	4.9×10^{31} erg	2.6×10^{31} erg

find a best agreement for a mean loop density $< n_e >_{rad} = 4.2 \times 10^{11}$ cm^{-3} and a loop number of $N_{loop} = 23$. This slight difference in best-fit parameters to the previously determined model parameters results from the fact that the simulated time profiles involve a convolution of time-extended loop activation rates $N(t)$ with broadband instrumental response functions $R(T)$, while our initial theoretical model was derived from an idealized concept with δ-functions in time and temperature. The best-fit parameters resulting from our forward-fitting approach are listed in Table III. The fits in Fig.12 demonstrate that our analytical model is able to reproduce the the observed peak delays for different instruments for the main flare peak. The secondary flare peak (visible at $\approx$ 10:40 UT in EUV) is not included in the fit, because it apparently is generated by a cooling function with a lower maximum temperature

T_2. Future modeling is envisioned with time-dependent variations of the physical parameters of the heating and cooling function.

Our analytical model contains total 11 free parameters: three parameters to characterize the temporal variation of the activated loops $N(t)$, i.e. $T_{P1}, \sigma_{T2}, N_{P1}$, four parameters related to the DEM distribution, $T_0, \sigma_{T1}, \sigma_{T2}, EM_0$, and four parameters of the plasma cooling function, $T_1, T_2, \tau'_{cond}, \tau_{rad}$. Alternatively, the parameters $EM_0, \tau'_{cond}, \tau_{rad}$ can be expressed by the three more basic physical parameters, r_{loop}, R_{arcade}, and $< n_e >_{rad}$.

4. Discussion and Conclusions

In this study we have applied a new technique to quantify the cooling of the flare plasma that takes advantage of multi-wavelength observations with comprehensive coverage over a broad temperature range ($T \approx 1 - 40$ MK) and attempts to reconstruct an instrument-independent differential emission measure distribution $dEM(T)/dT$ during the flare peak. The strength of this approach is the self-consistency of the obtained solution among different instruments, avoiding erroneous results due to the limited temperature range of single instruments, non-uniqueness of temperature filter ratios, or separation problems of thermal and nonthermal emission. We find a differential emission measure distribution during the flare peak that contains 99% of the flare plasma at temperatures $T \lesssim 35$ MK, which clearly rules out previous claims of flare temperatures in the order of $T \approx 200$ MK, based on filter ratios between the Yohkoh/HXT Lo and M1 channels (Masuda, 1994). Our analysis clearly reveals that the HXT/M1 channel (23-33 keV) represents a mixture of thermal and nonthermal emission, and that only a lower envelope (approximately proportional to the HXT/Lo channel profile F_{Lo}) to the fast time structures seen in the M1 channel flux, F_{M1}, can be attributed to thermal emission.

Our solution of the DEM distribution exhibits a peak at $T_0 \approx 10$ MK, indicating that the bulk of the heated flare plasma (evaporated from the chromosphere) has this temperature, while smaller amounts of mass are evaporated at lower and higher temperatures. If we make the assumption that (1) the flare loop filling occurs much faster (typically in the order of 30 s according to numerical simulations, e.g. (Mariska et al., 1989) than the flare plasma cooling (which is found occur here within > 420 s), and that (2) the temperature is monotonically falling during the cooling phase, we can invert the plasma cooling function $T(t)$ from the DEM distribution of the average loop and the peak time delays $t(T)$ observed in different instrumental temperature bands. We

find a plasma cooling function that drops from an initial temperature of $T \approx 30$ MK down to 1 MK within 780 s, where the cooling in the first phase down to 23 MK, lasting 188 s, is dominated by conductive cooling, while the second phase with cooling from 25 MK down to 1 MK is dominated by radiative cooling. For comparison, flare plasma cooling was modeled by Culhane et al. (1994) from Yohkoh/HXT and BCS data, and the data were found to be consistent with conductive cooling in the temperature range from 23 MK down to 11 MK, over a time period of 180 s. Because the electron densities are comparable in the two flares within a factor of $\lesssim 2$, the two obtained cooling functions are consistent in the first phase with dominant conductive cooling, while the second phase with dominant radiative cooling could not be reconstructed in the study by Culhane et al. (1994) due to the temperature restriction of BCS. Our result contradicts theoretical models that assume that conductive cooling mostly dominates over radiative cooling (Antiochos and Sturrock, 1978), but strongly supports models with dominant radiative cooling, e.g. (Antiochos, 1980), and models with initial conductive cooling followed by radiative cooling, e.g. (Cargill et al., 1995). Our observationally obtained plasma cooling function $T(t)$ has good similarity with theoretically obtained cooling functions, which typically reach a maximum of $T \approx 30$ MK within 200 s, and then cool down to $T = 1$ MK in the subsequent next 800 s, e.g. (Fisher and Hawley, 1995).

Our results on the filling factor has some interesting consequences about the unresolved fine structure of flare loops. From the emission measure modeling we found that some 23 loops with a radius of 0.9 Mm and an arcade radius of 17.5 Mm fully account for the observed emission measure at the flare peak time, assuming a mean electron density that is consistent with the observed radiative cooling. The fact that we counted roughly the same number of loops during this flare phase and resolved them spatially with TRACE (with a resolution of $\gtrsim 0.7$ Mm) means that these loops have a filling factor of heated plasma near to 100%. If these loops had a fine structure consisting of thinner threads, the thread density would be higher and should cool faster than the observed radiative cooling time, which is not the case. However, if we ask, what volume percentage of the flare arcade is filled with heated flare plasma, we obtain locally some 16%, which represents instantaneously only $\approx$ 4% of the total flare arcade volume.

We modeled and discussed in this study only the thermal aspects of the flare plasma in this well-observed Bastille-Day flare. We think that this analysis, which manages to reconcile the multi-wavelength observations to a reasonable degree, presents a solid basis for additional modeling that address further aspects, such as nonthermal hard X-ray

emission (Masuda et al., 2001) as well as magnetic field topology (Title et al., 2001) and modeling (Yan, 2001), (Bush et al., 2001).

Acknowledgements

We thank Richard W. Nightingale for assisting with TRACE data, Gregory L. Slater for support of Yohkoh/HXT data, and Samuel L. Freeland for special help with SSW and GOES software. The Yohkoh data used in this paper are taken by the Yohkoh mission of ISAS, Japan, which was prepared and is operated by the international collaboration of Japanese, US, and UK scientists under the support of ISAS, NASA, and SERC, respectively. The TRACE team includes scientists from Lockheed Martin Advanced Technology Center, Stanford University, NASA Goddard Space Flight Center, the University of Chicago, Montana State University, and the Harvard-Smithsonian Center for Astrophysics. GOES data are produced by the Space Environment Center (SEL) of the National Oceanic and Atmospheric Administration (NOAO). Work was supported by NASA contract NAS5-38099 (TRACE) and NAS8-00119 (SXT).

References

Alexander, D. and T. R. Metcalf. *The Astrophysical Journal*, 489: 442-455, 1997.

Antiochos,S. K. and P. A. Sturrock. *The Astrophysical Journal*, 220: 1137-1143, 1978.

Antiochos,S. K. *The Astrophysical Journal*, 241: 385-393, 1980.

Aschwanden, M. J., R. M. Bynum, T. Kosugi, H. H. Hudson, and R. A. Schwartz. *The Astrophysical Journal*, 487: 936-955, 1997.

Aschwanden, M. J., T. D. Tarbell, R. W. Nightingale, C. J. Schrijver, A. Title, C. C. Kankelborg, P. Martens, and H. P. Warren. *The Astrophysical Journal*, 535: 1047-1065, 2000.

Bush,R. et al. *Solar Physics*, (This issue) in press, 2001.

Cargill,P. J., J. T. Mariska, and S. K. Antiochos *The Astrophysical Journal*, 439: 1034-1043, 1995.

Carmichael,H., in AAS-NASA Symposium on Solar Flares, ed. W. N. Hess (NASA SP-50) p.451, 1964.

Culhane,J. L. et al. *Solar Physics*, 153: 307-336.

Feldman,U. *Phys.Scripta*, 46: 202-220, 1992.

Fisher,G. H. and Hawley,S. L. *The Astrophysical Journal*, 357: 243-258, 1995.

Freeland, S. L. and Handy, B. N. et al. *Solar Physics*, 182: 497-500, 1998.

Handy, B. et al. *Solar Physics*, 187: 229-260, 1999.

Masuda, S. *Hard X-ray Sources and the Primary Energy Release Site in Solar Flares*, PhD Thesis, Natl. Astornomical Obs., Mitaka, Tokyo 181, Japan.

Masuda, S. et al. *Solar Physics* (This Volume), subm.

Meyer,J. P. *Astrophys.J.Suppl.*, 57: 173-204, 1985.

Kopp,R. A. and Pneuman,G. W. *Solar Physics*, 50:85-98.
Kosugi, T. et al. *Solar Physics*, 136: 17-36, 1991.
Mariska,J. T., A. G. Emslie, and P. Li *The Astrophysical Journal*, 341: 1067-1074, 1989.
Title, A. et al. *Solar Physics* (This Volume), subm.
Rosner,R., W. H.Tucker, and G.S.Vaiana *The Astrophysical Journal* 220:643-665.
Sakao,T., Kosugi,T., Masuda,S., Inda,M., Makishima,K., Canfield,R. C., Hudson,H. S., Metcalf,T. R., Wuelser,J.-P., Acton,L. W., and Ogawara,Y. *Publ.Astron.Soc.Japan* 44:L83-L85, 1992.
Sturrock,P. A. *Nature* 211:695-697, 1966.
Tsuneta,S. et al. *Solar Physics*, 136: 37-61, 1991.
Tsuneta,S. *The Astrophysical Journal*, 456: 840-849, 1996.
Yan,Y., Y. Deng, M. Karlicky, Q. Fu, S. Wang, and Y.Liu *The Astrophysical Journal Letters*, 551:L115-L120, 2001.